Auger-Meitner and X-ray absorption spectra of ethylene cation: Insight from conical intersection dynamics

Bruno Nunes Cabral Tenorio,[*,†,§] Jacob Pedersen,[†,‖] Mario Barbatti,[‡,⊥] Piero Decleva,[¶] and Sonia Coriani[*,†]

†*DTU Chemistry - Department of Chemistry, Technical University of Denmark, Kemitorvet Bldg 207, DK-2800 Kongens Lyngby, Denmark*

‡*Aix-Marseille University, CNRS, ICR, Marseille, France*

¶*Istituto Officina dei Materiali IOM-CNR and Dipartimento di Scienze Chimiche e Farmaceutiche, Università degli Studi di Trieste, I-34121 Trieste, Italy*

§*Departamento de Química, Universidad Autónoma de Madrid and Instituto Madrileño de Estudios Avanzados en Nanociencia (IMDEA-Nanociencia), Madrid 28049, Spain*

‖*Department of Chemistry, Norwegian University of Science and Technology, N-7491 Trondheim, Norway*

⊥*Institut Universitaire de France, 75231, Paris, France*

E-mail: bruno.nunescabral@inv.uam.es; soco@kemi.dtu.dk

Abstract

We present a theoretical investigation into the near-edge X-ray absorption fine structure and the Auger-Meitner decay spectra of ethylene and its cation. Herein, we demonstrate that our method, coupled with the nuclear ensemble approach, successfully reproduces the natural bandwidth structure of the experimental resonant

Auger-Meitner decay spectra of ethylene, which is not very well reproduced within the Franck-Condon approximation. Furthermore, we have analyzed the Auger-Meitner decay spectra of the ethylene cation in the light of minimum energy conical intersection structures involving the two lowest cationic states (D_1 and D_0), providing valuable insights into the ultrafast D_1/D_0 relaxation dynamics. Our results suggest that Auger-Meitner electron spectroscopy can help elucidate the mechanism behind the initial 20 fs of the relaxation dynamics.

1 Introduction

Attosecond science is an emerging field that offers the ultimate time resolution necessary for studying and understanding dynamics at conical intersections (CIs).[1–3] Excited-state dynamics of polyatomic molecules often involve the coupling of vibrational and electronic degrees of freedom due to the breakdown of the Born-Oppenheimer approximation.[4] These processes are facilitated by CIs, which have emerged as the accepted mechanism for understanding the underlying time scales of ultrafast nonradiative processes. Schuurman and Stolow have recently touched upon the importance of including dynamics in this context and understanding CIs as a transition state of the excited state.[5] The advent of attosecond spectroscopy, and thus the toolbox to clock and map out sub-femtosecond dynamics makes such realization possible.

The relaxation dynamics of the ethylene cation $C_2H_4^+$ has gained significant attention due to its ultrafast nature. In particular, the photodynamics of the cation is known to proceed through conical intersections, but despite it being the simplest possible π radical system, the relaxation mechanism has been discussed for more than a decade.[6–12] In one of the most recent studies, Zinchenko et al.[8] identified the electronic relaxation from the first excited state of the ethylene cation (D_1) to its ground state (D_0) through a planar conical intersection. The most direct evidence of the electronic relaxation was the observation of a short-lived transient feature assigned to the D_1 state in both the experiment (attosecond

transient absorption spectroscopy measurements) and ab initio multiple spawning quantum dynamical simulations. Meanwhile, the particular absorption feature characteristic of the D_1 state overlaps with one of the ground state absorption features, thereby making the deconvolution of the spectra cumbersome.[8]

Auger-Meitner electron spectroscopy maps the electronic relaxation (nonradiative autoionization) mechanism of core vacant states into the kinetic energy of an ejected electron. In both normal and resonant Auger-Meitner electron spectroscopy (AES and RAES, respectively), the core orbital vacancy is refilled upon the relaxation of a valence electron and simultaneous ejection of another valence electron.[13–15] The techniques allow atomic and molecular decay channels to be probed directly, and much effort is currently being invested in the development of the methods both experimentally[16–18] and theoretically.[19–24]

The computation of Auger-Meitner decay spectra is very challenging because it requires the inclusion and treatment of an electron in the continuum, which cannot be modeled with the same square-integrable basis functions as the bound states.[25–27] We have recently presented a computational protocol for AES and RAES based on the restricted active space perturbation theory to second order (RASPT2) wave function parameterization and the one-center approximation (OCA), termed OCA-RASPT2.[23] The one-center approximation exploits the spatial locality of the Auger-Meitner decay process and essentially amounts to substituting the challenging and expensive exact two-electron bound-continuum integrals with pre-calculated one-center (atomic) two-electron integrals.[23,28,29]

Using pre-calculated integrals makes the OCA-RASPT2 protocol extremely cost-efficient without sacrificing the quality of the results. In particular, we have demonstrated the success of the protocol for a range of small to medium-sized molecules in previous work.[17,23,30] The low-cost efficiency of our implementation opens up the opportunity to perform time-resolved Auger-Meitner electron spectroscopy. Wang et al. have very recently proposed this to follow the O-H bond stretching in the water molecule.[31]

In this work, we revisit the investigation of the electronic relaxation mechanism of the

ethylene cation with Auger-Meitner electron spectroscopy. The purpose of our study is two-fold: First, we bring forward new evidence for the electronic relaxation mechanism of the ethylene cation, which we hope can help settle the ongoing discussion. In particular, Auger-Meitner electron spectroscopy brings forward the opportunity to follow the electronic relaxation through the conical intersection in a site-specific way, and our results clearly show a distinction between the two electronic states, thereby alleviating the problem of overlapping absorption features.[8] Second, we showcase as a proof-of-concept how Auger-Meitner electron spectroscopy can be applied to extract detailed information concerning the entanglement of the electronic and nuclear motion, and hereby hope to inspire and motivate the experimental X-ray community to invest in the development of time-resolved Auger-Meitner electron spectroscopy.

To benchmark the accuracy of our protocol, we have very recently investigated the Auger-Meitner decay of argon following primary ($1h$) and shake-up/shake-off satellite ($2h1p/2h$) core-ionized states.[32] Here, the parentheses denote the character of the initial states. Notably, the shake-up states of argon share a comparable electronic structure with the core-excited open-shell cations ($2h1p$) of the ethylene cation. The lack of vibrational degrees of freedom in an atom ensures direct probing of the electronic resonances, thereby making argon the perfect test system. Thus, given our successful simulation of the AES in shake-up states in argon, we are confident in the accuracy of our Auger-Meitner calculations on the ethylene cation.

The paper is organized as follows. The main components of the OCA-RASPT2 protocol are shortly detailed in Section 2. We then describe the computational approach in Section 3, and our results are presented and discussed in Section 4. Conclusions and outlook are provided in Section 5.

2 Theory

In the Wentzel approximation, the initial-state preparation (core-ionization in AES and core-excitation in RAES) and subsequent Auger-Meitner decay are considered as decoupled, and the total decay rate is described through the Fermi golden rule,[33,34]

$$\Gamma_{\mathrm{IF}} = \sum_{l,m} \Gamma_{\mathrm{IF};Elm}, \tag{1}$$

with $\Gamma_{\mathrm{IF};Elm}$ being the partial decay rate parameterized by the Wentzel ansatz,[35–37]

$$\Gamma_{\mathrm{IF};Elm} = 2\pi \left| \langle \Psi_{\mathrm{F};Elm} | \, \hat{H} - E_{\mathrm{I}} \, | \Psi_{\mathrm{I}} \rangle \right|^2 . \tag{2}$$

Here, $\Psi_{\mathrm{F};Elm}$ is the final state wave function, $\hat{H}$ is the molecular Hamiltonian, and E_{I} is the energy of the initial state wave function Ψ_{I}. The electron emission angular distribution has been assumed isotropic, and we sample over all possible angular momenta of the continuum electron.

The final state wave function is, within the single-channel approximation, an antisymmetrized product of the $(N-1)$-electron wave function (with N being the initial number of electrons) and a continuum orbital ϕ_{Elm}, characterized by the kinetic energy E and angular momentum quantum numbers l and m of the continuum electron[23,30]

$$\Psi_{\mathrm{F};Elm} = \hat{\mathcal{A}}(\Psi_{\mathrm{F}}^{N-1} \phi_{Elm}) \ , \tag{3}$$

where $\hat{\mathcal{A}}$ is an appropriate antisymmetrizer.

The OCA-RASPT2 protocol exploits the state interaction approximation, in which matrix elements between optimized molecular orbitals from separate RASPT2 calculations are evaluated efficiently due to pre-biorthogonalization of the two orbital sets. The separate orbital optimization ensures proper treatment of correlation effects within both the initial and final states.[38] The partial decay rate can, within the state interaction approximation,

be decomposed into a one-electron part $A_{\mathrm{IF};Elm}$ and a two-electron part $B_{\mathrm{IF};Elm}$

$$\Gamma_{\mathrm{IF};Elm} = 2\pi \left| A_{\mathrm{IF};Elm} + B_{\mathrm{IF};Elm} \right|^2 . \tag{4}$$

In the one-center approximation,[28,29] we neglect the one-electron term and substitute the exact two-electron bound-continuum integral in

$$B_{\mathrm{IF};Elm} = \langle \hat{a}^\dagger_{Elm} \Psi^{N-1}_{\mathrm{F}} | \, \hat{g} \, | \Psi^{N}_{\mathrm{I}} \rangle = \sum_{q,r,s} \langle \phi_{Elm} \phi_q | \, \hat{g} \, | \phi_r \phi_s \rangle \, \gamma^{\mathrm{IF}}_{qsr}. \tag{5}$$

with pre-calculated one-center integrals of the corresponding atom A for core-hole site c taken from Ref. 39,

$$\langle \phi_{Elm} \phi_c | \, \hat{g} \, | \phi_r \phi_s \rangle \simeq I^{A}_{Elm,c,r,s} \ . \tag{6}$$

In respect to Eq. (5), $\hat{a}^\dagger_{Elm}$ is the continuum electron creation operator, $\hat{g}$ is the two-electron Coulomb operator, $\{\phi_p, \phi_q, ...\}$ denotes the set of biorthogonalized molecular orbitals, and $\gamma^{\mathrm{IF}}_{qsr}$ is the two-particle Dyson matrix element,[23,30,38]

$$\gamma^{\mathrm{IF}}_{qsr} = \langle \Psi^{N-1}_{\mathrm{F}} | \, \hat{a}^\dagger_q \hat{a}_s \hat{a}_r \, | \Psi^{N}_{\mathrm{I}} \rangle \, , \tag{7}$$

where $\hat{a}^\dagger_q$ and $\hat{a}_\mu$ with $\mu \in \{s, r\}$ are the fermionic creation and annihilation operators, respectively. For more details on the OCA-RASPT2 protocol, please consult Tenorio et al.[23]

3 Computational details

Initial core-ionized states and final decay states have been computed with the restricted active space self-consistent field (RASSCF) approach[40] making use of the aug-cc-pVTZ[41] basis set. The restricted active space approach is based on a threefold division of the correlation orbital space, denoted RAS1, RAS2, and RAS3.[42] The active space was formed with both carbon $1s$ orbitals in the RAS1 subspace, followed by the valence-occupied orbitals $2a_g$ (C $2s$), $2b_{1u}$ (C

$2s$), $1b_{2u}$ (σ_{CH}), $3a_g$ (σ_{CC}), $1b_{3g}$ (σ_{CH}), $1b_{3u}$ (π), and the virtual orbitals $1b_{2g}$ (π^*), $4a_g$ (σ^*_{CC}), $2b_{2u}$ (σ^*_{CH}), $2b_{3g}$ (σ^*_{CH}) in the RAS2 subspace. Note that our orbital symmetry labels are obtained for the molecular plane oriented along the yz-axis. The active orbitals are shown in the supplementary Figure S1 together with the calculated valence photoelectron spectrum.

Core-excited states were computed by placing the pertinent core orbitals in the RAS1 space and enforcing single electron occupation in it by means of the HEXS projection technique.[43] The RASSCF wave functions have been corrected by the regularized multi-state restricted-active-space perturbation theory of the second-order (RMS-RASPT2) approach.[44] The RMS-RASPT2 approach has been recently introduced by Battaglia *et al.*[44] to fix the intruder-state problem in CASPT2/RASPT2 based on σ^p regularization and achieves stability near a CASSCF intersection.

To ensure consistency, we have not employed any point group symmetry in the calculations presented here. The final states of XAS spectra were obtained by state-averaging over 30 core-excited roots, while for Auger-Meitner spectra, the final states were obtained by state-averaging over 100 cationic states. The OpenMolcas program package[45] was utilized to perform the RASPT2 calculations of XAS and AES.

Additionally, we used the density functional theory restricted open-shell configuration interaction singles (DFT/ROCIS) method[46] implemented in the ORCA program package,[47] adopting the B3LYP functional,[48] and the def2-TZVP,[49] basis set to calculate the XAS of the ethylene cation. Similarly to the RASSCF/RASPT2 approaches, ground and excited states of $C_2H_4{}^+$ are calculated as pure doublet states at the DFT/ROCIS level,[46] avoiding the problem of spin contamination of, *e.g.*, regular unrestricted TD-DFT calculations. However, we do acknowledge that the reliability of DFT/ROCIS for applications on minimum energy conical intersection (MECI) structures may be limited, as it remains a single reference method.

Here, we simulate XAS and AES line widths using two distinct methodologies. In the first one, we broaden the calculated spectral lines computed with a fixed molecular (experimental) geometry by applying Lorentzian functions, using a system-specific line-width parameter

chosen to match the experimental bandwidth. The molecular experimental geometry of neutral ethylene was obtained from the Nist database.[50] Alternatively, we adopt the nuclear ensemble approach (NEA).[51] Within the NEA framework, the inherent bandwidth of the spectrum is determined through the sum of transitions calculated from an ensemble of nuclear geometries sampled from, for example, a Wigner distribution of harmonic vibrational modes. In this work, we employ Lorentzian functions with a line width of 0.1 eV for the NEA simulations.

4 Results and discussion

4.1 Neutral ethylene

In Figure 1, we present the XAS, AES and RAES of C_2H_4 and compare with experimental data.[52] The calculated carbon $1s$ excitation and ionization energies (IE's) are compiled in Table 1. Upon comparison with experimental reference values,[8,52] our computed excitation energies exhibit an overall redshift of a few tenths of an eV. For example, the calculated excitation energy of the first resonance $C_{1s}(1b_{1u}) \rightarrow \pi^*(1b_{2g})$ is 284.1 eV, while the experimental result is reported as 284.7 eV.[52] To rectify this discrepancy, we have uniformly shifted all computed energies of the spectra plotted in Figure 1 by +0.5 eV. This shift equally applies to the calculated XAS, RAES, and AES spectra.

Table 1: C_2H_4. Main XAS features from the simulated RASPT2 spectra on the ground-state equilibrium geometry.

Energy	Excited State		Exp.[52]
(eV)	Assignment	Symmetry	(eV)
284.1	$1b_{1u}^{-1}1b_{2g}^{1}$	B_{3u}	284.7
286.4	$1b_{1u}^{-1}4a_{g}^{1}$	B_{1u}	287.4
287.2	$1a_{g}^{-1}2b_{2u}^{1}$	B_{2u}	287.8
288.4	$1b_{1u}^{-1}2b_{3g}^{1}$	B_{2u}	289.3
290.6	IE(C_{1s}^{-1})		290.8

IE = ionization energy

Computed AES spectra of ethylene are presented in panels **b)** and **c)** of Figure 1. In panel

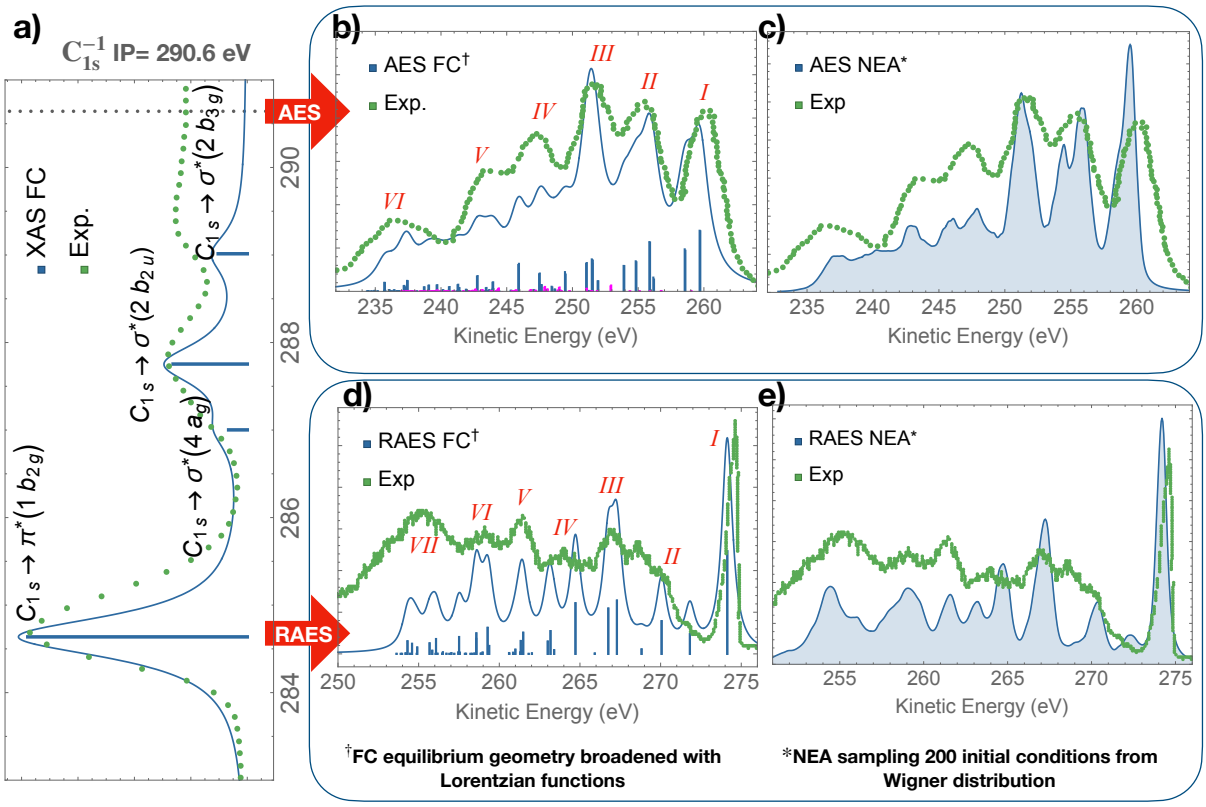

Figure 1: XAS, AES, and RAES of C_2H_4. All computed spectra have been shifted by +0.5 eV. The spectra computed in the FC regime shown in panels **a)**, **b)**, and **d)** were broadened with Lorentzian functions with fwhm = 0.6, 1.6, and 0.8 eV, respectively. Panels **c)** and **e)** were computed using the nuclear ensemble approach from 200 sampled initial conditions from a Wigner distribution.

b), we adopted the FC approximation by using the ground state geometry and convoluted the AES spectral lines using Lorentzian functions with a full width at half maximum (fwhm) of 1.6 eV. In panel **c)**, we employed the nuclear ensemble approach,[51] computed from 200 initial conditions sampled from a Wigner distribution of the harmonic vibrational modes of neutral ethylene. The sticks colored in blue and magenta in panel **b)** correspond to decay channels leading to singlet and triplet final states, respectively. The features identified as *I* through *IV* in panel **b)** are compiled in Table 2. Our assignments align quite well with the experimental data[53] and are also consistent with another computational study that employed the CBF/EOM-CCSD approach.[24] Interestingly, a close comparison with the experimental measurement reveals that the AES spectra obtained through the FC and nuclear ensemble approximations exhibit remarkably similar quality. This suggests that, in

this case, the computational cost associated with calculating AES spectra using the NEA may not be justified. However, this conclusion naturally depends on the molecular system and resolution of the experimental spectrum.

In panels **d)** and **e)** of Figure 1 are the resonant Auger-Meitner spectra computed for the core-excited state $C_{1s} \rightarrow \pi^*(1b_{2g})$. The features labeled from I to VII are assigned in Table 3. For the RAES of ethylene, we have again employed both the FC and nuclear ensemble approximations, using Lorentzian functions with fwhm of 0.8 eV for the FC spectrum and the same initial conditions outlined previously for AES. Notably, an evident improvement in the description of experimental features of the RAES spectrum is observed with the nuclear ensemble approach. Specifically, under the FC approximation, a distinct peak around 272 eV is observed, whereas the experiment shows no clear structure in this region. With the NEA, the peak intensity at 272 eV is considerably reduced. Moreover, the utilization of the NEA yields a significant improvement in the shapes of peaks V to VII when compared to the experiment. In particular, the double peak description obtained with the FC approximation for features VI and VII is shaped into a single broad peak with the NEA, in much better agreement with the bandwidths of the experiment.

In summary, the outcomes yielded by the RASPT2 computations, coupled with the one-center approximation for characterizing Auger-Meitner spectra of neutral ethylene, showcase a remarkable agreement with experimental data. With our computational approach validated on neutral ethylene, we now proceed to detail the XAS and AES spectra of the ethylene cation.

Table 2: C_2H_4. Main features of AES from the simulated RASPT2 spectra on the GS equilibrium geometry.

Peak	KE (eV)	Γ ($\times 10^{-4}$a.u.)	Assignment
I	259.3	3.14	$1b_{3u}^{-2}$
I	258.2	2.84	$1b_{3u}^{-1}1b_{3g}^{-1}$
II	255.5	2.44	$3a_{g}^{-1}1b_{3u}^{-1}$
II	254.6	2.21	$1b_{3u}^{-1}1b_{2u}^{-1}$
II	253.5	1.10	$3a_{g}^{-1}1b_{3g}^{-1}$
III	251.1	2.15	$1b_{2u}^{-1}1b_{3g}^{-1}$
III	250.6	1.99	$2b_{1u}^{-1}1b_{3u}^{-1}$
IV	247.0	1.28	$2b_{1u}^{-1}1b_{3g}^{-1}$
V	242.3	0.96	$2a_{g}^{-1}1b_{3u}^{-1}$
VI	236.8	0.70	$2a_{g}^{-1}1b_{3u}^{-1}$

KE = kinetic energy

Table 3: C_2H_4. Main features of RAES from the simulated RASPT2 spectra on the GS equilibrium geometry.

Peak	KE (eV)	Γ ($\times 10^{-4}$a.u.)	Assignment
I	273.6	6.38	$1b_{3u}^{-1}$
II	271.4	1.30	$1b_{3g}^{-1}$
II	269.5	1.06	$3a_{g}^{-1}$
III	268.3	0.70	$1b_{3u}^{-2}1b_{2g}^{1}$
IV	266.8	3.24	$1b_{3u}^{-1}1b_{3g}^{-1}1b_{2g}^{1}$
IV	266.2	2.90	$1b_{3u}^{-1}1b_{3g}^{-1}1b_{2g}^{1}$
V	264.2	2.50	$3a_{g}^{-1}1b_{3u}^{-1}1b_{2g}^{1}$
V	262.6	1.90	$1b_{2u}^{-1}1b_{3u}^{-1}1b_{2g}^{1}$
VI	260.8	0.86	$2a_{g}^{-1}$
VII	258.0	1.08	$3a_{g}^{-1}1b_{3u}^{-1}4a_{g}^{1}$
VII	257.2	1.25	$2b_{1u}^{-1}1b_{3u}^{-1}1b_{2g}^{1}$
VII	255.6	1.13	$3a_{g}^{-1}2b_{1u}^{-1}1b_{2g}^{1}$
VII	253.5	1.07	$2a_{g}^{-1}1b_{3u}^{-1}1b_{2g}^{1}$

KE = kinetic energy

4.2 Ethylene cation

In Figure 2, we present an overview of XAS and AES of $C_2H_4{}^+$, considering only the ground state of the cation, indicated as D_0 (b_{3u}^{-1}). The first step is the creation of a valence-ionized state, which is illustrated in panel **a)**. Panel **b)** shows the core-excited states reached upon excitation of a carbon $1s$ electron either to the singly occupied π ($1b_{3u}$) orbital or to the π^* ($1b_{2g}$) virtual orbital. Finally, Auger-Meitner decaying states of core states of $C_2H_4{}^+$ are illustrated in panel **c)**. We used yellow and purple background colors to distinguish between the Auger-Meitner decaying states resulting from the core states C $1s \rightarrow \pi(1b_{3u})$ and C $1s \rightarrow \pi^*(1b_{2g})$, respectively. The lower portions of Figure 2, panels **d)** and **e)**, report the calculated XAS and AES spectra. The photoelectron spectrum (PES) is given in Figure S1. The photoelectron intensities shown in Figure S1 are estimated by the squared norms of the corresponding Dyson orbitals.[54]

For the sake of simplicity, we will denote the low energy peak, associated with the C $1s \rightarrow \pi(1b_{3u})$ excitation, as P_1 and the high energy peak, corresponding to the C $1s \rightarrow \pi^*(1b_{2g})$ excitation, as P_2 (not to be confused with the P symmetry of an electronic state in atoms). Detailed assignments of the main orbital configurations in the XAS of $C_2H_4{}^+$ (based on the FC structure) can be found in Table 4.

Table 4: $C_2H_4{}^+$. Assignment of the main features in the simulated (RASPT2) XAS spectra at the GS equilibrium geometry for two different initial ionized states, namely D_0 ($1b_{3u}^{-1}$) and D_1 ($1b_{3g}^{-1}$).

Initial State		Final State	
Assignment	Energy (eV)	Assignment	Symmetry
$1b_{3u}^{-1}$	279.9	$1a_g^{-1}$ (P_1)	A_g
$1b_{3u}^{-1}$	286.1	$1b_{1u}^{-1}1b_{3u}^{-1}1b_{2g}^{1}$ (P_2)	A_g
$1b_{3u}^{-1}$	291.2	$1a_g^{-1}1b_{3u}^{-1}2b_{2u}^{1}$	B_{1g}
$1b_{3g}^{-1}$	277.5	$1b_{1u}^{-1}$ (P_1)	B_{1u}
$1b_{3g}^{-1}$	285.4	$1b_{1u}^{-1}1b_{3g}^{-1}1b_{2g}^{1}$ (P_2)	A_u
$1b_{3g}^{-1}$	289.9	$1a_g^{-1}1b_{3g}^{-1}2b_{2u}^{1}$	B_{1u}

The PES spectrum, see Figure S1, reveals the presence of two cationic states within the energy range of 10 to 13 eV. The ground state of the cation, D_0, corresponds to the

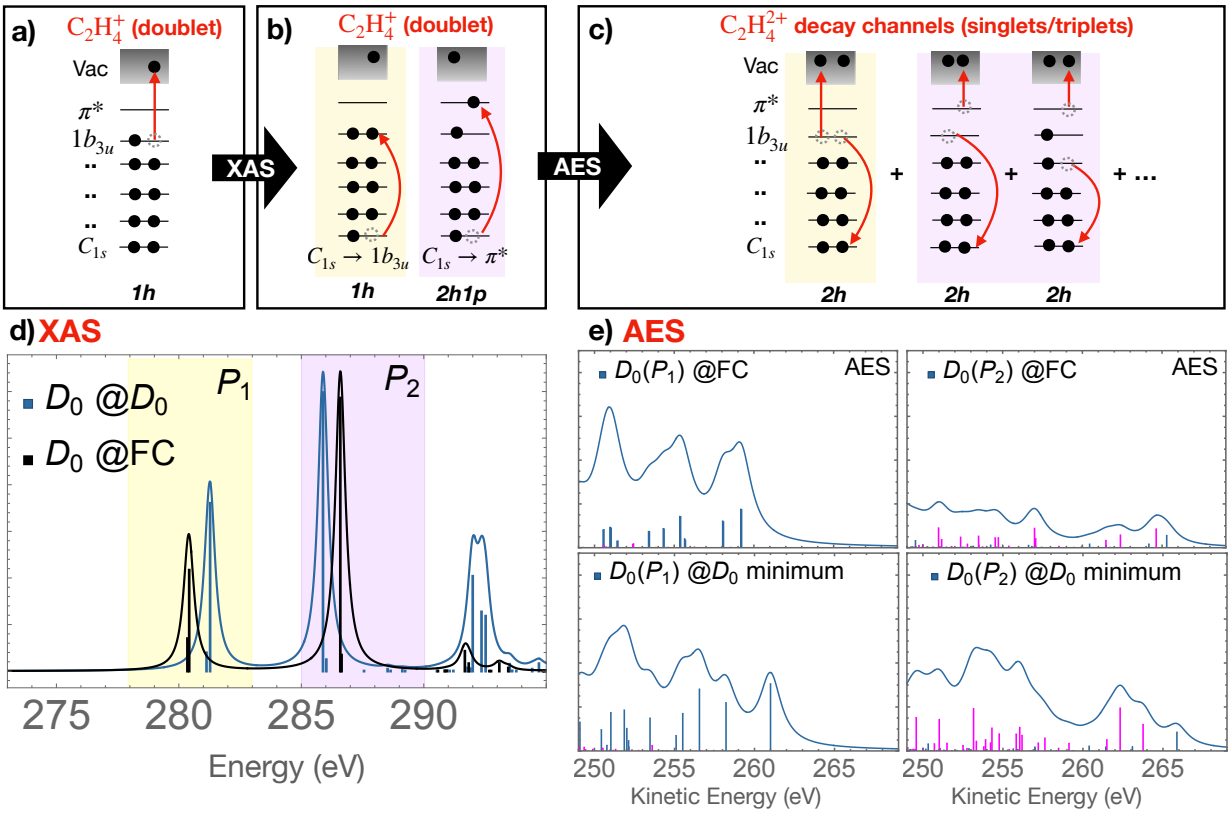

Figure 2: **a)** Illustration of the photoionization of a b_{3u} electron of C_2H_4, followed by **b)** the XAS and **c)** the AES of $C_2H_4^+$. In panels **b)** and **c)**, the XAS and AES are schematized from the point of view of the ground state of the ethylene cation, D_0. In panels **d)** and **e)**, we show the computed XAS and AES spectra of $C_2H_4^+$ stemming from both the P_1 and the P_2 core states. The spectra in **d)** and **e)** were broadened with Lorentzian functions with fwhm = 0.6 (XAS) and 1.6 eV (AES).

ionization of an electron in the $1b_{3u}$ orbital, exhibiting an ionization energy (IE) of around 10.1 eV. Subsequently, the first excited state of the cation, designated as D_1, emerges with an ionization energy of nearly 12.2 eV, corresponding to the removal of an electron from a $1b_{3g}$ orbital.

Within panel **d)**, we display the calculated XAS spectra of $C_2H_4^+$ both in the Franck-Condon (FC) regime (i.e., at the ground-state geometry of the neutral species), and utilizing the equilibrium geometry of D_0 as obtained from the work of Joalland et al.[6] It is noteworthy that the spectra simulated under the FC regime exhibit only relatively small deviations from those computed using the equilibrium geometry of D_0. The calculated P_1 peak associated with the C $1s \rightarrow \pi(1b_{3u})$ excitation, when utilizing the equilibrium geometry of D_0, displays

a blue shift of approximately 1 eV compared to the FC calculation. Conversely, the P_2 peak assigned to the C $1s \rightarrow \pi^*(1b_{2g})$ transition obtained with the equilibrium geometry of D_0 exhibits a red shift of roughly 1 eV relative to the FC calculation. These observations align well with the results reported in Ref. 8.

Lastly, within panel **e)**, we present the AES stemming from both the P_1 and the P_2 initial core states. These AES results were obtained for both the FC regime and the equilibrium geometry of D_0. Notably, P_1 corresponds to the same initial core-ionized state of the AES depicted in panel **b)** of Figure 1; hence, the spectra are identical. Consequently, for P_1, singlet decay channels (blue sticks) exhibit prevalence over triplet decay channels (magenta sticks). In the case of P_2, on the other hand, the situation is reversed, with triplet decay channels prevailing over singlet decay channels. Similar scenarios where there is a prevalence of triplet decay channels have been previously observed in the Auger-Meitner decay spectra of open-shell molecules, as shown for instance in Ref. 23 in the case of NO_2.

Distinct superpositions of cations can be achieved based on the conditions governing the formation of the initial wave packet, as demonstrated in a recent study by Lucchini et al.[7] In the present investigation, we direct our attention to a specific scenario involving the superposition of the D_0 and D_1 states, which has been exploited in Ref. 8.

In Figure 3, panel **a)**, we show a schematic representation of the core excitations of $C_2H_4^+$ for both the D_0 and D_1 states. In panel **b)**, we provide the calculated XAS and AES spectra for D_0 and D_1 in the Franck-Condon regime. Given that there is an approximate 2 eV separation between the peaks corresponding to the $1b_{3u}$ and $1b_{3g}$ ionizations in the PES spectrum, we anticipate the initial core-excitation C $1s \rightarrow 1b_{3u}$ to be nearly 2 eV higher in energy compared to C $1s \rightarrow 1b_{3g}$. This expectation is confirmed by the calculated XAS presented in panel **b)** of Figure 3.

Regarding the core excitation to the π^* $(1b_{2g})$ orbital, the situation is less clear. The XAS spectra resulting from the RASPT2 calculations in the FC regime displayed in panel **b)** of Figure 3 suggest that the corresponding C $1s \rightarrow \pi^*$ transition of D_1 is approximately

0.5 eV lower in energy than the same transition of D_0. Additional calculations using the DFT/ROCIS(B3LYP) approach, as presented in Figure S2, panel , reveal consistent trends for P_1. However, in contrast to the RASPT2 results, the position of C $1s \rightarrow \pi^*$ in D_1 obtained with DFT/ROCIS(B3LYP) is slightly higher in energy compared to the position of C $1s \rightarrow \pi^*$ in D_0.

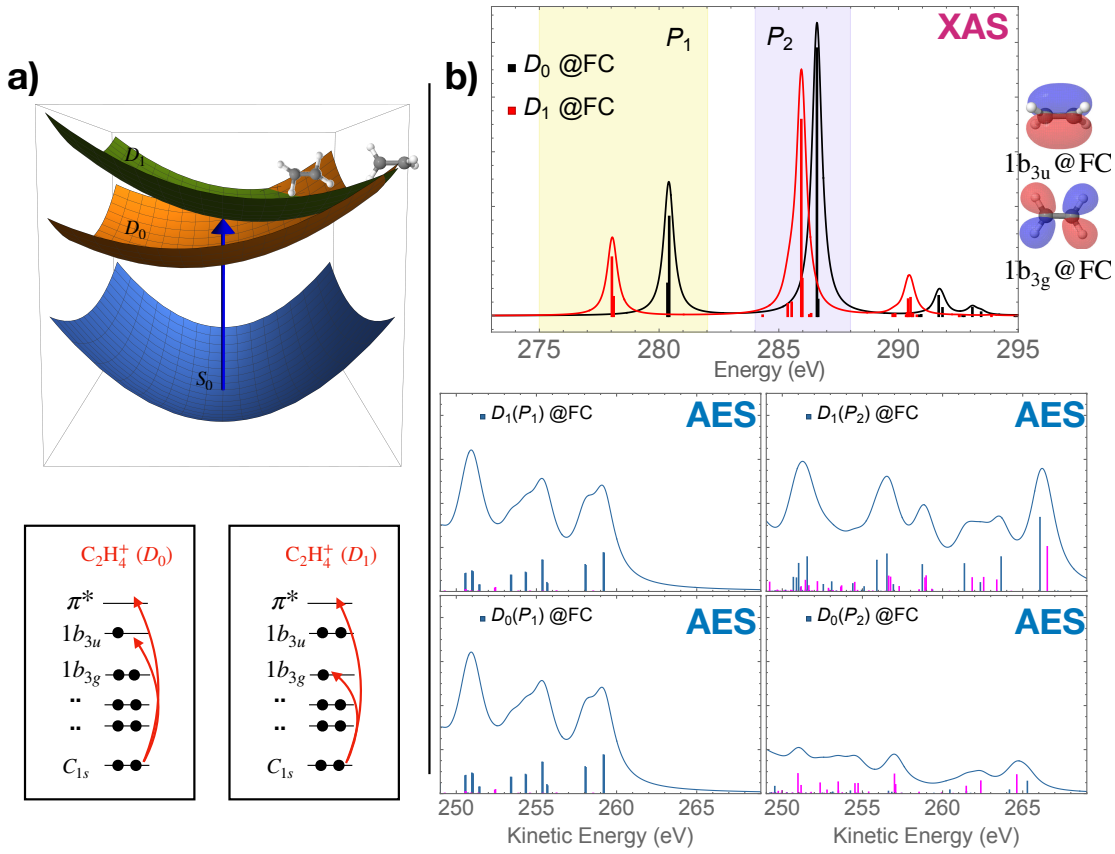

Figure 3: **a)** The cationic surfaces accessed from the neutral ground state S_0. The surfaces illustrate the competition between torsional and planar D_1/D_0 intersections. A schematic of the relevant core excitations from the D_0 and D_1 cationic states is shown at the bottom of panel **a)**. **b)** XAS and AES of $C_2H_4^+$ of D_0 ($1b_{3u}$) and D_1 ($1b_{3g}$) at the FC structure. The sticks were broadened with Lorentzian functions with fwhm = 0.6 and 1.6 eV, for XAS and AES, respectively.

Table 5 collects the excitation energies of P_1 and P_2 computed using the RASPT2 and DFT/ROCIS(B3LYP) methodologies. Additionally, it includes values obtained from Ref. 8 through calculations carried out at the DFT-MRCI/aug-cc-pVDZ level of theory. Apart from the DFT/ROCIS(B3LYP) offset relative to experimental values, which is rectified by shifting its energy values by 12 eV, a general agreement is observed for the excitation energies

Table 5: XAS of $C_2H_4^+$: core excitation energies in eV from RASPT2, DFT/ROCIS, and DFT-MRCI levels of theory computed for the D_0 and D_1 initial cationic states. In parenthesis, we show the DFT/ROCIS excitation energies shifted by +12 eV.

Peak	RASPT2	DFT/ROCIS(B3LYP)	DFT-MRCI[a]	Exp.[a]
		D_0@D_0		
P_1	280.8	268.1(280.1)	280.4	281
P_2	285.4	274.0(286.0)	285.6	286
		D_0@FC		
P_1	279.9	267.3(279.3)	279.8	
P_2	286.1	274.4(286.4)	286.0	
		D_1@FC		
P_1	277.5	265.9(277.9)	277.4	
P_2	285.4	274.7(286.7)	284.3	

[a]Results extracted from Ref. 8. The basis set used with DFT-MRCI was aug-cc-pVDZ.

of P_1 and P_2 across the electronic states and geometries. The noticeable disparity in our comparative analysis arises in relation to the vertical excitation energy of P_2 in the D_1 state. Based on the results from RASPT2 and DFT-MRCI,[8] it is evident that the excitation energy of P_2 in D_1 falls below the reference value of 286 eV, which is the experimental value associated with P_2 in the D_0 state. However, according to the DFT-MRCI calculations,[8] the excitation energy of P_2 in D_1 is approximately 1 eV lower than the prediction from RASPT2.

The experimental XAS of $C_2H_4^+$ discussed in Ref. 8 reveals a transient band, with a duration below 10 fs, centered around 284 eV. The authors have proposed that the abrupt shift of more than 1 eV as the electronic character switches from D_1 to D_0 at the Franck-Condon regime is pivotal for comprehending the D_1/D_0 ultrafast relaxation through a planar conical intersection. Based on the results from DFT-MRCI, the transient band around 284 eV can be explained by the wave packet motion of the D_1 state from the Franck-Condon point to the planar MECI. Conversely, this transient band cannot be accounted for by the wave packet motion of the D_1 state from the Franck-Condon point to the planar MECI, based on the results obtained from the RASPT2 (or DFT/ROCIS) calculations. As indicated by the RASPT2 findings, the ultrafast relaxation between the D_1 and D_0 states via a planar conical intersection would remain concealed because the energy difference between the D_1 and D_0 states at the Franck-Condon point or at the relaxed geometry of D_0 is relatively small.

Consequently, this proximity in energy levels could obscure the D_1/D_0 ultrafast relaxation process through planar conical intersections.

In Ref. 6, Joalland et al. found competing relaxation pathways for various cationic states of $C_2H_4^+$ which entail two distinct families of conical intersections. These intersections are associated with minimum energy structures exhibiting planar and twisted geometries. Through the application of the *ab initio* multiple spawning method, the authors inferred from the collection of spawning events that, in the case of an initially populated D_1 state, as much as 90% of the related population transfer occurs via the planar conical intersection mechanism. Conversely, only approximately 10% of the initial distribution undergoes decay through the twisted conical intersection pathways. Moreover, the pathways mediated by torsional motion induce important backspawned population transfer promoted by hindered rotations. Structures of MECIs involved in non-adiabatic transitions calculated using the analytic non-adiabatic coupling method at the CASPT2 level of theory are available from Ref. 6. Using these structures along with their corresponding population transfers as outlined in Ref. 6 (specifically, 69% for a_1, 21% for a_2, and 10% for b, where a_1 and a_2 represent planar MECIs and b signifies a twisted MECI), we performed computations of XAS and AES for $C_2H_4^+$ at the geometries of these MECIs. The XAS calculations are presented in Figure 4. Note that in Figure 4 the XAS spectral intensities have been scaled by their corresponding population transfers.

As mentioned earlier, the P_2 peaks (> 285 eV) computed based on the geometries of the planar MECIs a_1 and a_2 exhibit substantial overlap with the energy of the P_2 peaks calculated using the relaxed geometry of D_0 (≈ 286 eV). The P_1 peaks calculated using the same geometries of planar MECIs are observed to have lower energy compared to the energy of P_1 obtained using the relaxed geometry of D_0 (≈ 281 eV), which align with the computational results presented in Ref. 8. Furthermore, we observe a remarkable similarity between the XAS spectra acquired for the D_0 and D_1 electronic states, as presented in the top and bottom panels of Figure 4, respectively. This resemblance is to be anticipated due

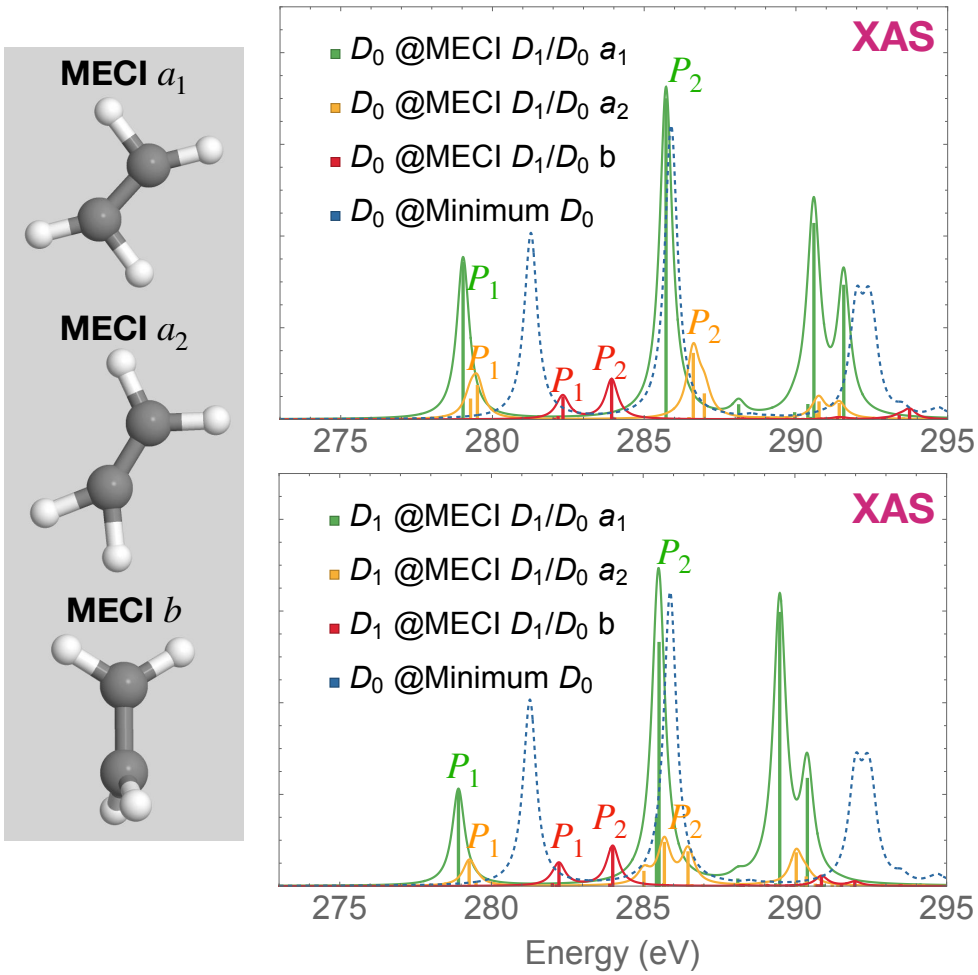

Figure 4: XAS spectra of $C_2H_4^+$ in D_0 (top) and D_1 (bottom) at MECI structures. The XAS spectra are weighted by the corresponding population transfer associated with each MECI, i.e., 69% for a_1, 21% for a_2, and 10% for b. The sticks were broadened with Lorentzian functions with fwhm = 0.6 eV.

to the degeneracy of both electronic states at the MECIs.

An interesting finding emerges from the XAS spectra computed using the twisted MECI b. Specifically, we observe that the energies of P_1 and P_2 obtained using the geometry of the MECI b are approximately 282 and 284 eV, respectively. This observation is significant since among all the MECI structures, only the structure of the MECI b provides energies that correspond to the transient absorption band observed experimentally around 284 eV.[8] Such observation leads us to suggest that the experimental transient absorption band centered around 284 eV might be indicative of D_1/D_0 relaxation dynamics through a twisted conical intersection. In the supplementary Figure S2 panel **b)**, we assessed the XAS of $C_2H_4^+$ at the

geometries of MECIs utilizing the DFT/ROCIS(B3LYP) approach. The findings obtained from DFT/ROCIS(B3LYP) exhibit slight discrepancies in comparison to the RASPT2 results of Figure 4. Nonetheless, the significant observation that only the structure of the MECI **b** yields intensity below 284 eV remains consistent. Moreover, in Figure 5, we evaluated the XAS of $C_2H_4^+$ in the D_1 state across ten interpolated points that span the path connecting the FC structure to the twisted MECI *b*, utilizing a geodesic procedure.[55] From Figure 5, one can follow the redshift of peak P_2 coinciding with the variation in the CH_2 torsion.

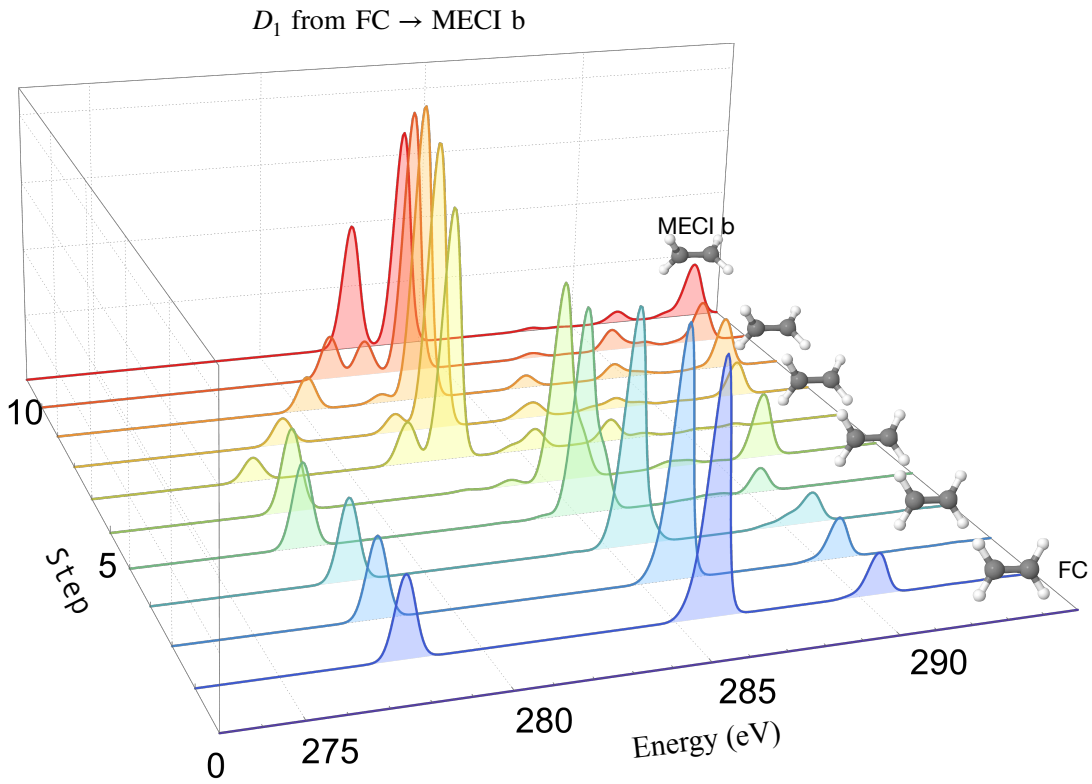

Figure 5: XAS of $C_2H_4^+$ in D_1 evaluated on ten interpolated points connecting the FC structure to the twisted MECI *b* using a geodesic procedure.[55]

Additionally, as illustrated in panel **B** of Figure 2 in Ref. 8, the temporal evolution of the experimental normalized intensity with pump-probe delay, integrated over the band centered around 284 eV, undergoes rapid decay [$\tau_1 = (6.8 \pm 0.2)$ fs] followed by a subsequent increase, culminating in a secondary peak around 30 fs, before attenuating again beyond 50 fs. This observation aligns with the conclusions presented by Joalland et al.,[6] where

pathways facilitated by torsional motion induce backspawned population transfer driven by hindered rotations. Conversely, such backspawned population transfers are not expected for relaxation pathways mediated by planar conical intersections.

The results and discussions presented thus far bring to light some questions regarding the appropriateness of XAS as a standalone technique to definitively unravel the intricate dynamics occurring at the conical intersections of the ethylene cation. Ideally, one would rely on more than one technique to extract as much information as possible from such an intricate mechanism. Such an approach would enable a better understanding of the dynamics at conical intersections. Thereby, we propose using Auger-Meitner electron spectroscopy as a supplemental technique in connection to XAS to maximize the extraction of valuable information and provide a more comprehensive understanding of the process.

The AES spectra showcased in Figure 6 distinctly illustrate differences when computed using the structures of the planar MECIs a_1 and a_2, as well as the structure of the twisted MECI b. Our proposed approach involves conducting AES measurements resonant with the positions of peaks P_1 and P_2 of the twisted MECI b, namely around 282 and 284 eV, respectively.

Around 282 eV, the Auger-Meitner spectra obtained from the planar MECI structures a_1 and a_2, along with the minimum energy structure of D_0, exhibit no intensity above 261 eV. In contrast, the structure of the twisted MECI b reveals a pronounced peak observed above 265 eV. This strong peak serves as a distinctive marker that can aid in distinguishing between planar and twisted MECIs, consequently facilitating the tracking of the structural region where relaxation dynamics occur. Alternatively, one could measure the Auger-Meitner spectrum around 284 eV—that is, at the center of the transient absorption band observed experimentally in Ref. 8. In this scenario, the planar structures exhibit a relevant intensity distribution extending up to 266 eV. Conversely, the structure of twisted MECI b does not display significant intensity above 261 eV.

The differences observed in the AES spectra, whether computed using planar or twisted

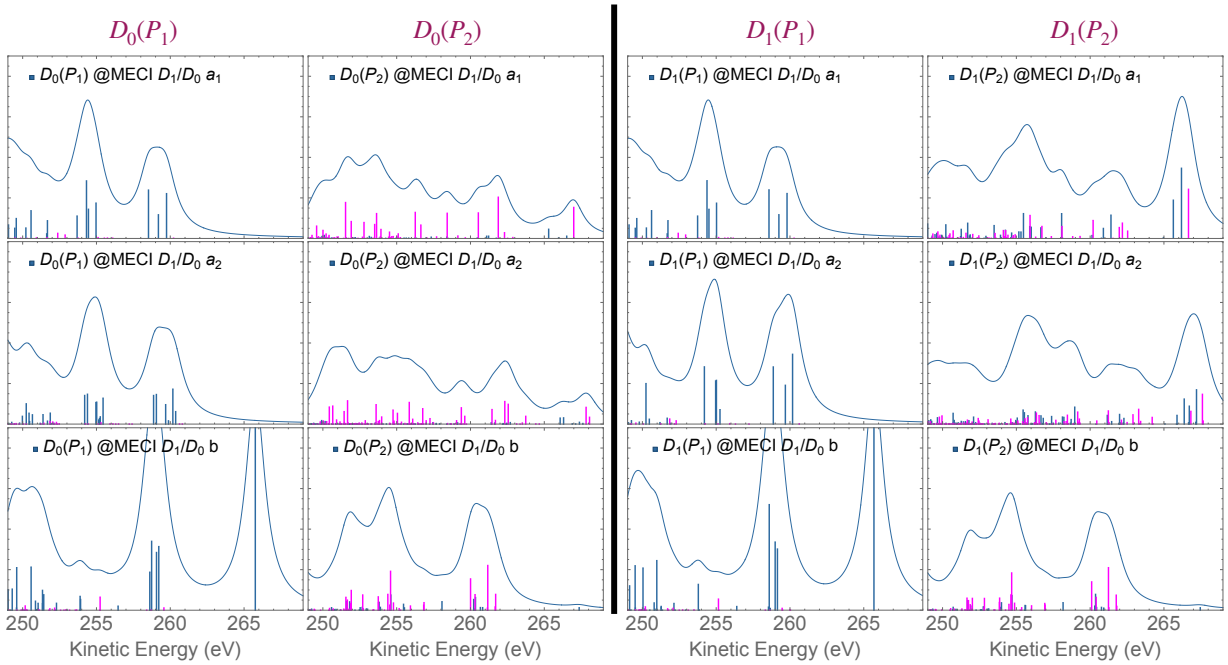

Figure 6: AES spectra of $C_2H_4^+$ in D_0 (*left*) and D_1 (*right*) at MECI structures. Each AES spectrum was computed in resonance with the P_1 or P_2 peak of the corresponding MECI structure (see in Fig. 4). The sticks were broadened with Lorentzian functions with fwhm = 1.6 eV.

MECI geometries, can serve as valuable indicators for distinguishing the D_1/D_0 relaxation mechanism based on the structural characteristics of the involved conical intersections. Such information adds an additional layer of insight to the XAS measurements of Ref. 8.

5 Conclusions

By combining theoretical calculations and comparison with experimental data, this study provides additional insights into the mechanisms governing the transition from the excited D_1 state to the electronic ground state D_0 of the ethylene cation. Our computational protocol, mainly based on the RASPT2 approach, has been initially successfully validated by calculating XAS and Auger-Meitner decay spectra of neutral ethylene. In this regard, we have demonstrated that the nuclear ensemble approach improves the description of the spectral features in resonant Auger-Meitner spectra. However, these improvements are not as noticeable in the non-resonant Auger-Meitner spectra due to the broader line widths in exper-

imental AES data. Overall, our RASPT2 computational protocol coupled with the one-center approximation for characterizing Auger-Meitner spectra achieved very good agreement with experimental XAS and Auger-Meitner measurements on neutral ethylene.

Additionally, the utilization of distinct computational methods, such as RASPT2 and DFT/ROCIS(B3LYP), has enabled the investigation of electronic states and geometries of $C_2H_4^+$, revealing nuanced trends in peak energies and spectral intensities. These trends, notably observed in the XAS and AES spectra, allowed us to identify key structures, such as planar and twisted MECIs, and their possible roles in the relaxation pathways. Crucially, the significance of structures like the twisted MECI *b* and their relation to transient absorption bands observed experimentally in Ref. 8 adds valuable insight into the ultrafast relaxation dynamics of $C_2H_4^+$. The potential of AES measurements, resonant with specific peak positions, has been highlighted as a complementary technique to distinguish and track relaxation mechanisms, enhancing the amount of information derived from XAS measurements alone.

In summary, we have showcased the promise of combining theoretical calculations of XAS and Auger-Meitner spectra with experimental data to unravel the dynamics at conical intersections and contribute to a more comprehensive understanding of the relaxation pathways within the ethylene cation. We hope that our findings serve as a catalyst for inspiring new experimental investigations, particularly time-resolved Auger-Meitner electron spectroscopy shedding light on the intricate interplay between electronic states and conical intersections on $C_2H_4^+$.

Supplementary information

The supplementary information contains a schematic representation of molecular orbitals in the active space, valence photoelectron spectrum, and DFT/ROCIS(B3LYP) calculated XAS spectra.

Acknowledgements

We gratefully acknowledge invaluable discussion with Dr. Prof. Hans Jakob Wörner (ETH Zürich). This work was carried out with support from the European Union's Horizon 2020 Research and Innovation Programme under the Marie Skłodowska-Curie Individual Fellowship (B.N.C.T., Grant Agreement 101027796) and from the Independent Research Fund Denmark–Natural Sciences, DFF-RP2 Grant No. 7014-00258B (S.C. and B.N.C.T.). J.P. acknowledges support from the Technical University of Denmark and DTU Chemistry within the Alliance Ph.D. Programme, from the Knud Højgaards Fond (Grant No. 23-02-2571), and from William Demant Fonden (Grant No. 23-3137). The European Cooperation in Science and Technology, COST Action CA18222, *AttoChem*, is also acknowledged.

Conflict of interest

The authors declare no conflict of interest.

References

(1) Hentschel, M.; Kienberger, R.; Spielmann, C.; Reider, G. A.; Milosevic, N.; Brabec, T.; Corkum, P.; Heinzmann, U.; Drescher, M.; Krausz, F. Attosecond metrology. *Nature* **2001**, *414*, 509–513.

(2) Haessler, S.; Caillat, J.; Boutu, W.; Giovanetti-Teixeira, C.; Ruchon, T.; Auguste, T.; Diveki, Z.; Breger, P.; Maquet, A.; Carré, B.; Taïeb, R.; Salières, P. Attosecond imaging of molecular electronic wavepackets. *Nature Physics* **2010**, *6*, 200–206.

(3) Xiao, Y.; Feng, C.; Liu, B. Generating Isolated Attosecond X-Ray Pulses by Wavefront Control in a Seeded Free-Electron Laser. *Ultrafast Science* **2022**, *2022*.

(4) Wörner, H. J.; Bertrand, J. B.; Fabre, B.; Higuet, J.; Ruf, H.; Dubrouil, A.;

Patchkovskii, S.; Spanner, M.; Mairesse, Y.; Blanchet, V.; Mével, E.; Constant, E.; Corkum, P. B.; Villeneuve, D. M. Conical Intersection Dynamics in NO_2 Probed by Homodyne High-Harmonic Spectroscopy. *Science* **2011**, *334*, 208–212.

(5) Schuurman, M. S.; Stolow, A. Dynamics at conical intersections. *Annu. Rev. Phys. Chem.* **2018**, *69*, 427–450.

(6) Joalland, B.; Mori, T.; Martínez, T. J.; Suits, A. G. Photochemical Dynamics of Ethylene Cation $C_2H_4^+$. *J. Phys. Chem. Lett.* **2014**, *5*, 1467–1471.

(7) Lucchini, M.; Mignolet, B.; Murari, M.; Gonçalves, C. E. M.; Lucarelli, G. D.; Frassetto, F.; Poletto, L.; Remacle, F.; Nisoli, M. Few-Femtosecond $C_2H_4^+$ Internal Relaxation Dynamics Accessed by Selective Excitation. *J. Phys. Chem. Lett.* **2022**, *13*, 11169–11175.

(8) Zinchenko, K. S.; Ardana-Lamas, F.; Seidu, I.; Neville, S. P.; van der Veen, J.; Lanfaloni, V. U.; Schuurman, M. S.; Wörner, H. J. Sub-7-femtosecond conical-intersection dynamics probed at the carbon *K*-edge. *Science* **2021**, *371*, 489–494.

(9) Allison, T. K.; Tao, H.; Glover, W. J.; Wright, T. W.; Stooke, A. M.; Khurmi, C.; van Tilborg, J.; Liu, Y.; Falcone, R. W.; Martínez, T. J.; Belkacem, A. Ultrafast internal conversion in ethylene. II. Mechanisms and pathways for quenching and hydrogen elimination. *J. Chem. Phys.* **2012**, *136*, 124317.

(10) van Tilborg, J.; Allison, T. K.; Wright, T. W.; Hertlein, M. P.; Falcone, R. W.; Liu, Y.; Merdji, H.; Belkacem, A. Femtosecond isomerization dynamics in the ethylene cation measured in an EUV-pump NIR-probe configuration. *J. Phys. B: At. Mol. Opt. Phys.* **2009**, *42*, 081002.

(11) Ludwig, A.; Liberatore, E.; Herrmann, J.; Kasmi, L.; López-Tarifa, P.; Gallmann, L.; Rothlisberger, U.; Keller, U.; Lucchini, M. Ultrafast Relaxation Dynamics of the Ethylene Cation $C_2H_4^+$. *J. Phys. Chem. Lett.* **2016**, *7*, 1901–1906.

(12) Ingle, R. A.; Banerjee, A.; Bacellar, C.; Barillot, T. R.; Longetti, L.; Coreno, M.; de Simone, M.; Zuccaro, F.; Poletto, L.; Miotti, P.; Röder, A.; Stolow, A.; Schuurman, M. S.; Odelius, M.; Chergui, M. Carbon K-edge x-ray emission spectroscopy of gas phase ethylenic molecules. *J. Phys. B: At. Mol. Opt. Phys.* **2022**, *55*, 044001.

(13) Matsakis, D.; Coster, A.; Laster, B.; Sime, R. A renaming proposal: The Auger–Meitner effect. *Phys. Today* **2019**, *72*, 10.

(14) Svensson, S. Soft x-ray photoionization of atoms and molecules. *J. Phys. B: At. Mol. Opt. Phys.* **2005**, *38*, S821–S838.

(15) Piancastelli, M. N.; Marchenko, T.; Guillemin, R.; Journel, L.; Travnikova, O.; Ismail, I.; Simon, M. Hard x-ray spectroscopy and dynamics of isolated atoms and molecules: a review. *Rep. Prog. Phys.* **2019**, *83*, 016401.

(16) Wolf, T. J.; Paul, A. C.; Folkestad, S. D.; Myhre, R. H.; Cryan, J. P.; Berrah, N.; Bucksbaum, P. H.; Coriani, S.; Coslovich, G.; Feifel, R., et al. Transient resonant Auger–Meitner spectra of photoexcited thymine. *Faraday Discuss.* **2021**, *228*, 555–570.

(17) Schnack-Petersen, A. K.; Tenorio, B. N. C.; Coriani, S.; Decleva, P.; Troß, J.; Ramasesha, K.; Coreno, M.; Totani, R.; Röder, A. Core spectroscopy of oxazole. *J. Chem. Phys.* **2022**, *157*, 214305.

(18) Li, S.; Driver, T.; Rosenberger, P.; Champenois, E. G.; Duris, J.; Al-Haddad, A.; Averbukh, V.; Barnard, J. C.; Berrah, N.; Bostedt, C., et al. Attosecond coherent electron motion in Auger-Meitner decay. *Science* **2022**, *375*, 285–290.

(19) Inhester, L.; Burmeister, C. F.; Groenhof, G.; Grubmüller, H. Auger spectrum of a water molecule after single and double core ionization. *J. Chem. Phys.* **2012**, *136*, 144304.

(20) Skomorowski, W.; Krylov, A. I. Feshbach-Fano approach for calculation of Auger decay rates using equation-of-motion coupled-cluster wave functions. I. Theory and implementation. *J. Chem. Phys.* **2021**, *154*, 012001.

(21) Grell, G.; Kühn, O.; Bokarev, S. I. Multireference quantum chemistry protocol for simulating autoionization spectra: Test of ionization continuum models for the neon atom. *Phys. Rev. A* **2019**, *100*, 042512.

(22) Grell, G.; Bokarev, S. I. Multi-reference protocol for (auto)ionization spectra: Application to molecules. *J. Chem. Phys.* **2020**, *152*, 074108.

(23) Tenorio, B. N. C.; Voß, T. A.; Bokarev, S. I.; Decleva, P.; Coriani, S. Multireference Approach to Normal and Resonant Auger Spectra Based on the One-Center Approximation. *J. Chem. Theory Comput.* **2022**, *18*, 4387–4407.

(24) Matz, F.; Nijssen, J.; Jagau, T.-C. Ab initio investigation of the Auger spectra of methane, ethane, ethylene, and acetylene. *J. Phys. Chem. A* **2023**, *127*, 6147–6158.

(25) Tenorio, B. N. C.; Coriani, S.; Rocha, A. B.; Nascimento, M. A. C. In *Molecular Photoionization and Photodetachment Cross Sections Based on L^2 Basis Sets: Theory and Selected Examples*; Glushkov, A. V., Khetselius, O. Y., Maruani, J., Brändas, E., Eds.; Advances in Methods and Applications of Quantum Systems in Chemistry, Physics, and Biology; Springer International Publishing: Cham, 2021; pp 151–179.

(26) Tenorio, B. N. C.; Nascimento, M. A. C.; Coriani, S.; Rocha, A. B. Coupled Cluster Study of Photoionization and Photodetachment Cross Sections. *J. Chem. Theory Comp.* **2016**, *12*, 4440–4459.

(27) Tenorio, B. N. C.; Nascimento, M. A. C.; Rocha, A. B.; Coriani, S. Lanczos-based equation-of-motion coupled-cluster singles-and-doubles approach to the total photoionization cross section of valence excited states. *J. Chem. Phys.* **2019**, *151*, 184106.

(28) Siegbahn, H.; Asplund, L.; Kelfve, P. The Auger electron spectrum of water vapour. *Chem. Phys. Lett.* **1975**, *35*, 330–335.

(29) Fink, R. Theoretical autoionization spectra of $1s \rightarrow \pi^*$ excited N_2 and N_2O. *J. Electron. Spectros. Relat. Phenomena* **1995**, *76*, 295–300.

(30) Tenorio, B. N. C.; Møller, K. B.; Decleva, P.; Coriani, S. Disentangling the resonant Auger spectra of ozone: overlapping core-hole states and core-excited state dynamics. *Phys. Chem. Chem. Phys.* **2022**, *24*, 28150–28163.

(31) Wang, C.; Gong, M.; Cheng, Y.; Kimberg, V.; Liu, X.-J.; Vendrell, O.; Ueda, K.; Zhang, S. B. Time-Resolved Resonant Auger Scattering Clocks Distortion of a Molecule. *J. Phys. Chem. Lett.* **2023**, *14*, 5475–5480.

(32) Pedersen, J.; Decleva, P.; Coriani, S.; Tenorio, B. N. C. Description of the KLL Auger–Meitner decay spectra of argon following primary and satellite core-ionized states. *J. Chem. Phys.* **2023**, *159*, 024121.

(33) Dirac, P. A. M. The Quantum Theory of the Emission and Absorption of Radiation. *Proc. R. Soc. Lond. A* **1927**, *114*, 243–265.

(34) Fermi, E. *Nuclear Physics*; Chicago: University of Chicago Press, 1950; p 142.

(35) Wentzel, G. Über strahlungslose Quantensprünge. *Z. Phys.* **1927**, *43*, 524–530.

(36) Manne, R.; Åberg, T. Koopmans' theorem for inner-shell ionization. *Chem. Phys. Lett.* **1970**, *7*, 282–284.

(37) Manne, R.; Ågren, H. Auger transition amplitudes from general many-electron wavefunctions. *Chem. Phys.* **1985**, *93*, 201–208.

(38) Tenorio, B. N. C.; Decleva, P.; Coriani, S. Multi-reference approach to the computation of double core-hole spectra. *J. Chem. Phys.* **2021**, *155*, 131101.

(39) McGuire, E. J. *K*-Shell Auger Transition Rates and Fluorescence Yields for Elements Be-Ar. *Phys. Rev.* **1969**, *185*, 1–6.

(40) Olsen, J.; Roos, B. O.; Jørgensen, P.; Jensen, H. J. A. Determinant based configuration interaction algorithms for complete and restricted configuration interaction spaces. *J. Chem. Phys.* **1988**, *89*, 2185–2192.

(41) Woon, D. E.; Dunning, T. H. Gaussian basis sets for use in correlated molecular calculations. IV. Calculation of static electrical response properties. *J. Chem. Phys.* **1994**, *100*, 2975–2988.

(42) Malmqvist, P.-Å.; Pierloot, K.; Shahi, A. R. M.; Cramer, C. J.; Gagliardi, L. The restricted active space followed by second-order perturbation theory method: Theory and application to the study of CuO_2 and Cu_2O_2 systems. *J. Chem. Phys.* **2008**, *128*, 204109.

(43) Delcey, M. G.; Sørensen, L. K.; Vacher, M.; Couto, R. C.; Lundberg, M. Efficient calculations of a large number of highly excited states for multiconfigurational wavefunctions. *J. Comput. Chem.* **2019**, *40*, 1789–1799.

(44) Battaglia, S.; Fransén, L.; Fdez. Galván, I.; Lindh, R. Regularized CASPT2: an Intruder-State-Free Approach. *J. Chem. Theory Comput.* **2022**, *18*, 4814–4825.

(45) Manni, G. L.; Fdez. Galván, I.; Alavi, A.; Aleotti, F.; Aquilante, F.; Autschbach, J.; Avagliano, D.; Baiardi, A.; Bao, J. J.; Battaglia, S.; Birnoschi, L.; Blanco-González, A.; Bokarev, S. I.; Broer, R.; Cacciari, R.; Calio, P. B.; Carlson, R. K.; Carvalho Couto, R.; Cerdán, L.; Chibotaru, L. F.; Chilton, N. F.; Church, J. R.; Conti, I.; Coriani, S.; Cuéllar-Zuquin, J.; Daoud, R. E.; Dattani, N.; Decleva, P.; de Graaf, C.; Delcey, M. G.; Vico, L. D.; Dobrautz, W.; Dong, S. S.; Feng, R.; Ferré, N.; Filatov(Gulak), M.; Gagliardi, L.; Garavelli, M.; González, L.; Guan, Y.; Guo, M.; Hennefarth, M. R.;

Hermes, M. R.; Hoyer, C. E.; Huix-Rotllant, M.; Jaiswal, V. K.; Kaiser, A.; Kaliakin, D. S.; Khamesian, M.; King, D. S.; Kochetov, V.; Krośnicki, M.; Kumaar, A. A.; Larsson, E. D.; Lehtola, S.; Lepetit, M.-B.; Lischka, H.; López Ríos, P.; Lundberg, M.; Ma, D.; Mai, S.; Marquetand, P.; Merritt, I. C. D.; Montorsi, F.; Mörchen, M.; Nenov, A.; Nguyen, V. H. A.; Nishimoto, Y.; Oakley, M. S.; Olivucci, M.; Oppel, M.; Padula, D.; Pandharkar, R.; Phung, Q. M.; Plasser, F.; Raggi, G.; Rebolini, E.; Reiher, M.; Rivalta, I.; Roca-Sanjuán, D.; Romig, T.; Safari, A. A.; Sánchez-Mansilla, A.; Sand, A. M.; Schapiro, I.; Scott, T. R.; Segarra-Martí, J.; Segatta, F.; Sergentu, D.-C.; Sharma, P.; Shepard, R.; Shu, Y.; Staab, J. K.; Straatsma, T. P.; Sørensen, L. K.; Tenorio, B. N. C.; Truhlar, D. G.; Ungur, L.; Vacher, M.; Veryazov, V.; Voss, T. A.; Weser, O.; Wu, D.; Yang, X.; Yarkony, D.; Zhou, C.; Zobel, J. P.; Lindh, R. The OpenMolcas Web: A Community-Driven Approach to Advancing Computational Chemistry. *J. Chem. Theory Comput.* **2023**,

(46) Roemelt, M.; Maganas, D.; DeBeer, S.; Neese, F. A combined DFT and restricted open-shell configuration interaction method including spin-orbit coupling: Application to transition metal L-edge X-ray absorption spectroscopy. *J. Chem. Phys.* **2013**, *138*, 204101.

(47) Neese, F. Software update: The ORCA program systemVersion 5.0. *WIREs Comput. Mol. Sci.* **2022**, *12*, e1606.

(48) Stephens, P. J.; Devlin, F. J.; Chabalowski, C. F.; Frisch, M. J. Ab Initio Calculation of Vibrational Absorption and Circular Dichroism Spectra Using Density Functional Force Fields. *J. Phys. Chem.* **1994**, *98*, 11623–11627.

(49) Schäfer, A.; Horn, H.; Ahlrichs, R. Fully optimized contracted Gaussian basis sets for atoms Li to Kr. *J. Chem. Phys.* **1992**, *97*, 2571–2577.

(50) NIST Computational Chemistry Comparison and Benchmark Database, NIST Standard Reference Database Number 101. Release 22, May 2022.

(51) Crespo-Otero, R.; Barbatti, M. Spectrum simulation and decomposition with nuclear ensemble: formal derivation and application to benzene, furan and 2-phenylfuran. *Theor. Chem. Acc.* **2012**, *131*, 1237.

(52) McLaren, R.; Clark, S. A. C.; Ishii, I.; Hitchcock, A. P. Absolute oscillator strengths from K-shell electron-energy-loss spectra of the fluoroethenes and 1,3-perfluorobutadiene. *Phys. Rev. A* **1987**, *36*, 1683–1701.

(53) Rye, R. R.; Madey, T. E.; Houston, J. E.; Holloway, P. H. Chemical-state effects in Auger electron spectroscopy. *J. Chem. Phys.* **2008**, *69*, 1504–1512.

(54) Tenorio, B. N. C.; Ponzi, A.; Coriani, S.; Decleva, P. Photoionization Observables from Multi-Reference Dyson Orbitals Coupled to B-Spline DFT and TD-DFT Continuum. *Molecules* **2022**, *27*, 1203.

(55) Zhu, X.; Thompson, K. C.; Martínez, T. J. Geodesic interpolation for reaction pathways. *J. Chem. Phys.* **2019**, *150*, 164103.